Enhanced backscatter and unsaturated blue wavelength shifts in F-doped fused silica optical fibers exposed to extreme neutron radiation damage

Christian M. Petrie* **and Daniel C. Sweeney**

Oak Ridge National Laboratory, P.O. Box 2008, Oak Ridge, TN 37831, USA

**petriecm@ornl.gov*

Abstract

Amorphous fused silica (a-SiO_2) optical fibers, with and without inscribed Bragg gratings, were interrogated using infrared (~1550 nm) optical backscatter reflectometry during ~25 days of intense neutron irradiation to a fast (energy > 0.1 MeV) neutron fluence of ~10^{21} n/cm^2, or ~1.5 atomic displacements per atom. The reflected light amplitudes in Ge-doped core telecommunications fiber dropped below detection limits (>15 dB attenuation) within 3 days of irradiation (~10^{20} fast n/cm^2). Amplitudes from a pure silica core, F-doped silica cladding fiber reached equilibrium levels ~1.5–2 dB *higher* than pre-irradiation values, whereas Bragg gratings inscribed in the same fiber using a femtosecond laser (point-by-point method) suffered > 45 dB attenuation. Blue wavelength shifts were initially consistent with previous radiation-induced compaction models but increased linearly with increasing neutron fluence (no evidence of saturation) beyond 10^{20} n/cm^2 and exceeded 0.6%, which corresponds to >1,000 °C drift if used to measure temperature changes.

1. Introduction

Optical fibers have long been considered as candidates for signal transmission and sensing in high-radiation environments, including satellite and space applications, high energy physics facilities, and containment or confinement structures surrounding fusion and fission nuclear reactors [1]. Significant work has been dedicated to understanding the fundamental point defects introduced in amorphous fused silica (a-SiO_2) caused by ionization or displacement damage, including dependencies of the radiation-induced attenuation (RIA) on photon wavelength (λ), dose, dose rate, temperature, and fiber composition [2-4]. RIA is the primary limitation of fiber optics for nuclear applications and is most significant in the ultraviolet to visible spectrum, although some absorption bands possess tails that extend into the near-infrared. Additionally, atomic displacements caused by fast neutron irradiation of a-SiO_2 are known to compact the amorphous structure, which eventually reaches an equilibrium metamict phase with a 2–3% increase in density and a 0.6–0.8% increase in refractive index after accumulating a fast neutron fluence >10^{20} n_{fast}/cm^2 [5-7]. These changes in density and refractive index manifest as a drift in optical fiber-based sensors such as fiber Bragg gratings (FBGs) [8], but this drift is expected to saturate once the metamict structure is fully formed. Previous works provide more details regarding radiation effects on different types of FBGs [9, 10], with a significant portion of the experimental data originating from gamma or X-ray irradiations with a total ionizing dose of ~GGy or less.

Extension of fiber optics to extreme-dose applications such as in-core sensing in fission-based nuclear reactors has long been met with skepticism based on the poor radiation tolerance of telecommunication fibers even at relatively low levels (1 kGy) of ionizing dose from gamma rays. Telecommunications fibers contain dopants such as P and Ge that are known to significantly increase RIA, becoming intolerable for higher-dose applications [11]. Fluorine-doped silica cladding fibers with either a pure silica core or lower doping of F in the core (relative to that of the cladding) have shown promise. For example, RIA < 10 dB/m was measured near 1500 nm in some cases during gamma and moderate neutron fluence (~10^{20} n_{fast}/cm^2 or lower) irradiation [12-14]. However, at >10^{18} n_{fast}/cm^2, increased infrared RIA was observed, which increased with increasing wavelength beyond ~1,000 nm. The origins of this infrared RIA have been attributed to increased vibrational absorption caused by fast neutron-induced compaction of the a-SiO_2 structure [8, 15], which should also reach an equilibrium once the metamict structure is fully formed at neutron fluences on the order of 10^{20} n_{fast}/cm^2 [5].

To date, testing of radiation-hardened fibers to neutron fluences approaching or exceeding 10^{20} n_{fast}/cm^2 has been performed only using fibers with inscribed FBGs or other laser-induced scattering enhancements to compensate for RIA. Grating amplitudes decreased by ~6 dB and the Bragg wavelength drifted by ~0.3% during irradiation up to ~5×10^{20} n_{fast}/cm^2 [16]. Similar ~10 dB reductions in backscattered light amplitude were observed in radiation-hardened fibers with laser-enhanced Rayleigh backscatter (RBS) irradiated to ~6×10^{20} n_{fast}/cm^2 [17]. The latter work did not report radiation-induced wavelength shifts relative to the initial pre-irradiation spectra, potentially because of poor correlations that resulted after the signal attenuation. The challenge in these cases is that it is not possible to separate fundamental RIA and compaction-induced changes in a-SiO_2 properties (density, refractive index) from radiation effects on the gratings or other signal enhancements. The critical gaps in assessing the suitability of radiation-hardened, F-doped fiber optics for extreme nuclear environments (>10^{21} n_{fast}/cm^2 or >1 atomic displacement per atom, dpa) include the following objectives: (1) determining whether the infrared RIA and wavelength shifts reach an equilibrium or otherwise remain tolerable, (2) identifying the mechanisms driving infrared RIA and wavelength shifts, and (3) evaluating whether FBGs or other backscatter enhancements suffer from additional radiation effects beyond those in the fiber itself.

This work summarizes experimental measurements recorded during the continuous interrogation of optical fibers during intense neutron irradiation at the highest steady-state fast neutron flux and fluence ever reported in the literature. Multiple fiber types with and without inscribed FBGs were tested to separate the effects of radiation on the fiber transmission vs. the grating reflectivity. The interrogation method allowed for evaluation of spatially dependent reflected signal amplitudes (e.g., RIA) and spectral shifts.

2. Methodology

Pure a-SiO_2 core, F-doped a-SiO_2 cladding single-mode fibers—SM1250SC(9/125) from Fibercore—were continuously interrogated using optical backscatter reflectometry (OBR using the 4600 model from Luna Innovations) during intense neutron irradiation in the High Flux Isotope Reactor (HFIR) [18, 19] at Oak Ridge National Laboratory. Fig. 1 shows the experimental configuration. Multiple fibers were tested (see Table 1) with and without inscribed FBGs (~0.5% reflectivity) and are hereinafter referred to as F-FBG and F-RBS, respectively, denoting the fiber dopant (F) and light scattering mechanism (i.e., FBG or RBS). A relatively low grating reflectivity was chosen to minimize reflection losses from the FBGs and improve signal transmission to the

FBGs at the end of the array. The FBGs (Type II) were inscribed through the fiber coating using a femtosecond laser following the common point-by-point approach. A standard telecommunications single-mode fiber (SMF-28e+ from Corning) with a Ge-doped a-SiO_2 core and pure a-SiO_2 cladding was also included in the test as a reference (denoted as Ge-RBS).

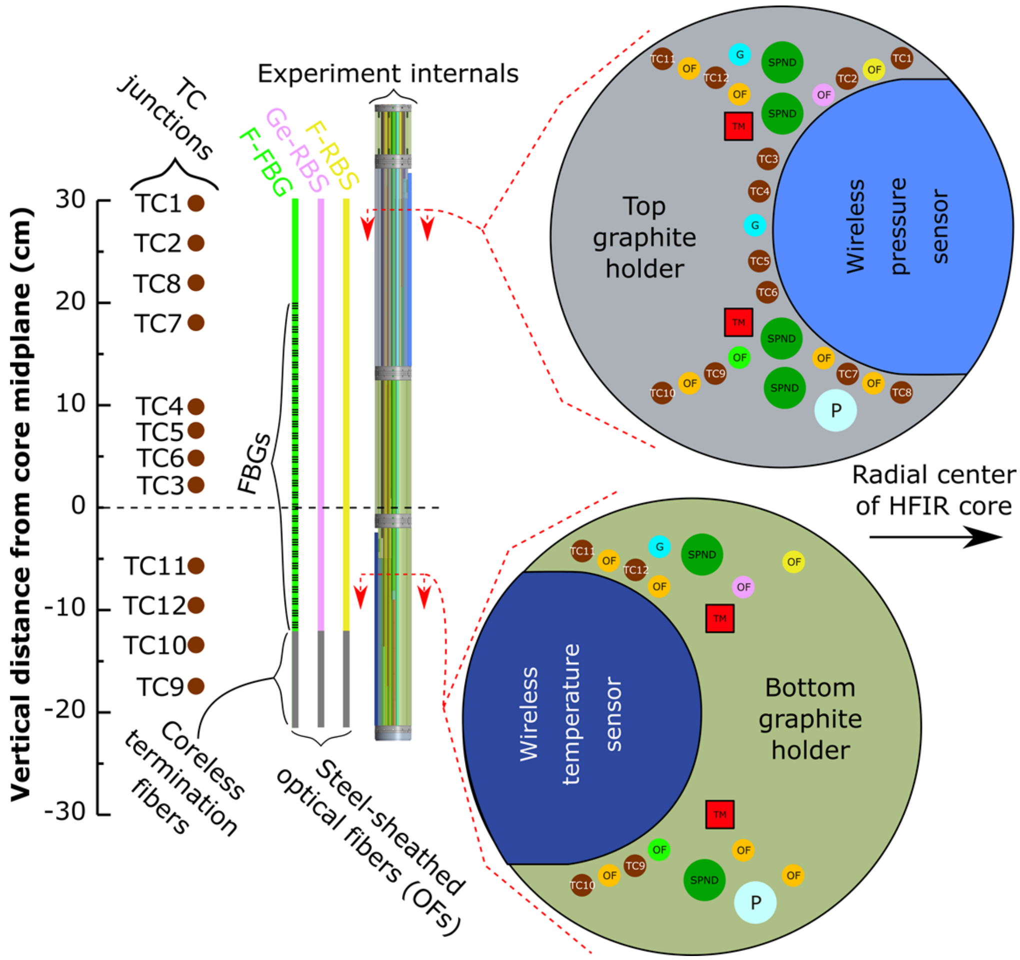

Fig. 1. Experimental configuration showing the locations of all thermocouples (TCs) and optical fibers (OFs), including the FBGs in the F-FBG fiber and the coreless termination fibers that were spliced to the end of each fiber. Other sensors were included in the experiment but are not discussed herein. Those include other OFs, wireless temperature and pressure sensors, passive temperature monitors (TMs), self-powered neutron detectors (SPNDs), a purge gas line (P), and multiple control gas lines (G). The two graphite holders have different geometries to accommodate leads from sensors that terminate at lower elevations. TC2 and TC8 were faulted from the start of the experiment and were therefore not used.

The OBR system uses a tunable laser to sweep over a range of wavelengths (1530.0–1571.7 nm) and performs Fourier analyses to determine the backscattered light amplitude vs. position along the fiber [20]. Using a sliding spatial window, data from select regions can be transformed back into the spectral domain and cross-correlated with an unperturbed reference scan made before irradiation to determine spatially dependent spectral (wavelength) shifts [21]. Data were acquired from each fiber every 5 minutes and processed using previously established adaptive reference techniques [22-24] that adjust the reference scan based on the correlation coefficient to more accurately resolve incremental spectral shifts that can be summed to determine larger spectral shifts.

Table 1. Optical fibers included in the irradiation test.

Fiber	Vendor	Part Number	Core	Cladding	Coating	Gratings
F-RBS	Fiber-core	SM1250SC (9/125)P	Ø9 µm SiO_2	Ø125 µm F-doped SiO_2	Ø155 µm polyimide	N/A
F-FBG						28 fs gratings, ~1 cm spacing, ~0.5% reflectivity, 1548 nm center wavelength
Ge-RBS	Corning	SMF-28e+	Ø8.2 µm Ge-doped SiO_2	Ø125 µm SiO_2	Ø242 µm acrylate	N/A

Near the reactor core midplane, the time-averaged thermal neutron flux (energy < 1 eV) and gamma dose rate were 8.8×10^{14} $n_{thermal}/cm^2/s$ and 33 MGy/hr, respectively, for all fibers. After 25.3 effective full-power days of irradiation, the maximum integrated thermal neutron fluence was 2.0×10^{21} $n_{thermal}/cm^2$, and the total ionizing dose was 20 GGy. The fast neutron flux (energy > 0.1 MeV) and fluence near the core midplane were in the range of 4.5×10^{14} $n_{fast}/cm^2/s$ and 1.0×10^{21} n_{fast}/cm^2 but varied slightly for each fiber due to their radial distance from the center of the reactor core. Assuming displacement threshold energies of 15 eV for Si and 28 eV for O [25], the calculated displacement damage dose near the core midplane was in the range of 1.4–1.5 dpa. Fig. A1 in the Appendix shows the spatial variations in fast neutron fluence and dose at the end of the experiment, for positions along each fiber > −10 cm. The fiber temperature (i.e., ~150–400 °C; see Fig. A2 in the Appendix) was independently monitored using 10 Type N thermocouples (locations shown in Fig. 1).

3. Results

3.1 Backscattered amplitudes

Fig. 2 shows the reflected signal amplitude from all three fibers vs. fast neutron fluence with the location relative to the reactor core midplane as a parameter. The amplitudes are relative to those obtained with a gold reflector attached to the OBR system. Positions farther from the core midplane were exposed to a lower neutron fluence because of the spatial variation in neutron flux. The semi-transparent shadings indicate the standard error of the mean measured amplitudes for each position and fast neutron fluence. Standard errors were obtained by taking the standard deviation of 521 data points that were measured within the 1 cm wide sensor gauge length, for each reported location, and then dividing by $\sqrt{521}$ to obtain the standard error of the mean. In this way, the standard error quantifies how well the mean amplitude, taken over a discrete gauge length (sample), is representative of the true mean amplitude that is backscattered from a given position.

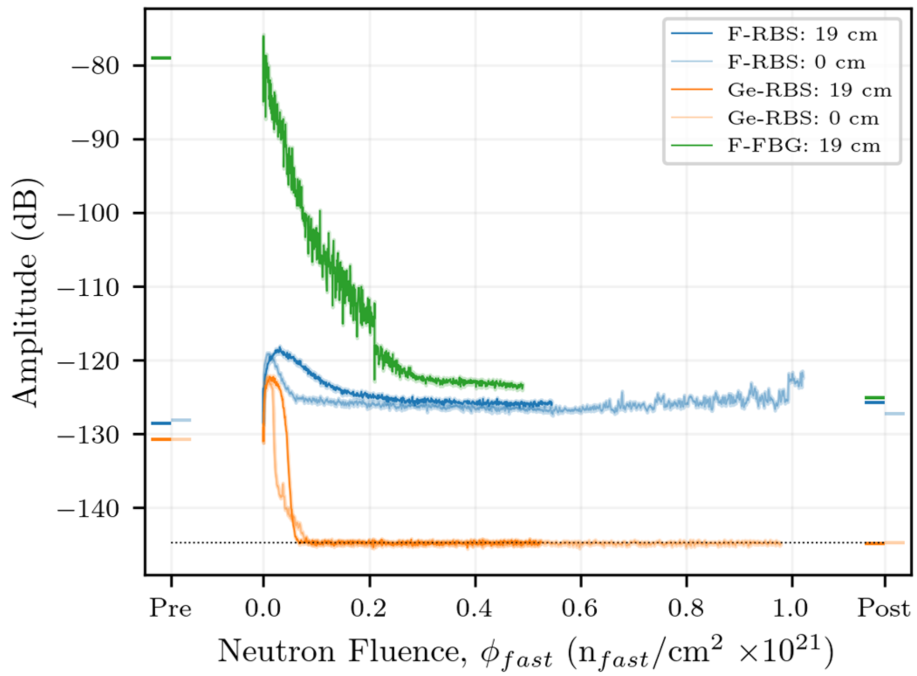

Fig. 2. Reflected signal amplitude vs. fast neutron fluence for each fiber at various locations. Amplitudes are also shown pre- and post-irradiation. The horizontal dashed line indicates the noise floor of the OBR system and the semi-transparent shadings indicate the standard error of the mean for each amplitude measurement.

All RBS amplitudes initially increased by ~10 dB during the first ascent to full reactor power up to ~10^{19} n_{fast}/cm^2, followed by a decrease in amplitude. As expected from previous RIA measurements [11], the Ge-RBS amplitudes decreased most significantly and approached the system noise floor within < 3 effective full power days of irradiation (<10^{20} n_{fast}/cm^2). The decrease in amplitude for F-RBS was much less significant. In fact, the amplitudes approached an equilibrium value that remained ~1.6 dB greater than the pre-irradiation amplitudes over the entire test.

The initial increases in amplitude can be explained by Fresnel reflections caused by compaction-induced increases in refractive index that varied along the length of the fiber as a result of spatial variations in neutron fluence. Similar reflections have been observed previously during neutron irradiation [14]. The refractive index has previously been shown to approach an equilibrium value when the fast neutron fluence is on the order of 10^{19} n_{fast}/cm^2 [5], which reduced the Fresnel reflections near the reactor midplane as the refractive index profile became more uniform. As the neutron fluence increased farther above the core, Fresnel reflections became more significant in these regions, causing the maximum reflected amplitude to shift to locations farther above the core (see Fig. 3). The large reflection peaks in Fig. 3 near −10 and −20 cm—which are particularly evident for the F-RBS and Ge-RBS fibers—are caused by reflections that occur at the interface between the fiber and a coreless termination fiber and the end of the termination fiber, respectively.

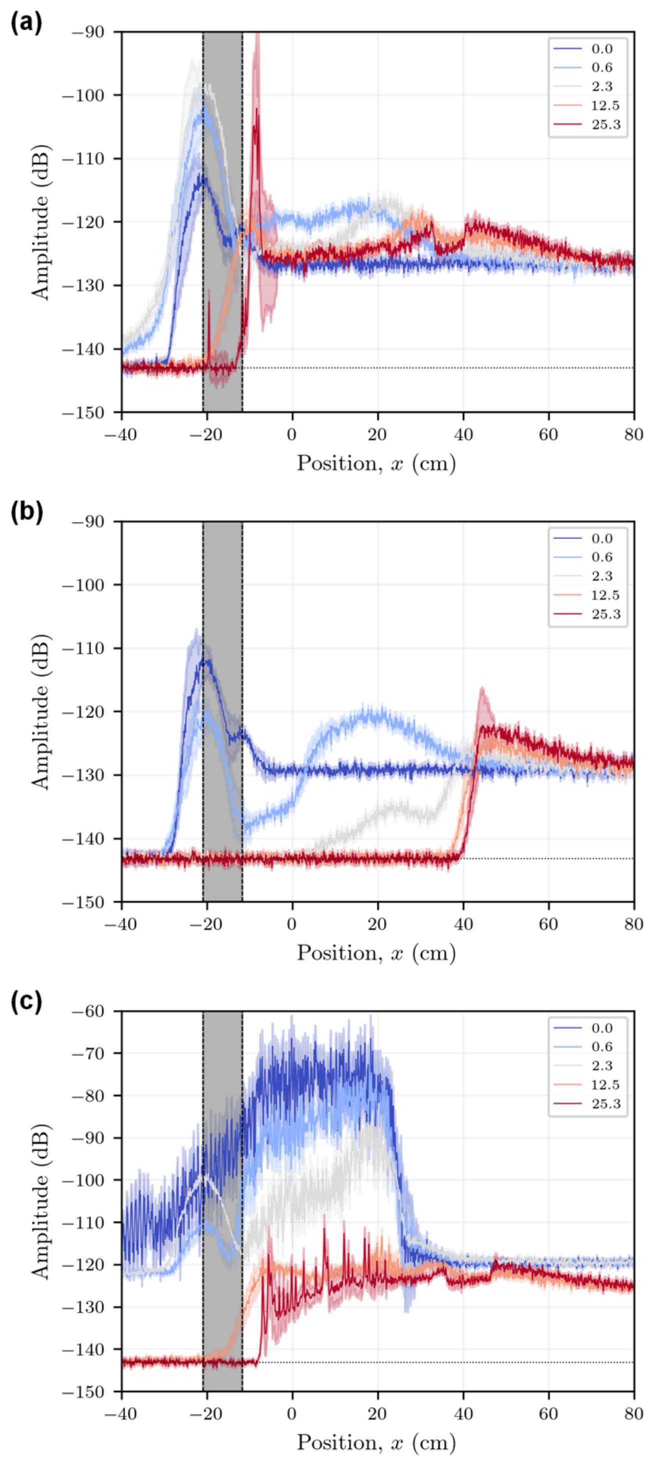

Fig. 3. Reflected signal amplitude vs. axial position relative to reactor core midplane at various effective full power days (indicated in the legends) for the (a) F-RBS, (b) Ge-RBS, and (c) F-FBG fibers. The regions that include the coreless termination fibers that were spliced to the ends of each sensing fiber are indicated with grey shading. Horizontal dashed lines indicate the noise floor of the OBR system and the semi-transparent shadings indicate the standard error of the mean for each amplitude measurement.

3.2 Spectral shifts

Fig. 4 shows local shifts in the reflected wavelength from the F-RBS and F-FBG fibers vs. fast neutron fluence; the locations relative to the reactor core midplane are indicated in the figure legends. Additional data are provided in Fig. A4 and Fig. A5 in the Appendix. Wavelength shifts are relative to the times when the reactor reached full power, and shifts during reactor startup and shutdown are not accounted for. Wavelength shifts could not be resolved in the Ge-RBS fiber due to the high RIA. Blue wavelength shifts >10 nm (0.63%) were measured, and the magnitudes of the wavelength shifts continued to increase with increasing fast neutron fluence with no evidence of saturation up to 10^{21} n_{fast}/cm^2. The fact that the trends in the measured shifts are the same with and without FBGs provides greater confidence in the shifts determined from the F-RBS fiber using adaptive reference techniques. The estimated wavelength shifts caused by changes in temperature and radiation-induced compaction (and the effects of compaction on refractive index [8]) are also shown. For neutron fluences on the order of ~10^{19} n_{fast}/cm^2, the compaction model shows relatively good agreement with the experimental results for the positions with higher neutron flux (≤10 cm). The disagreement at positions >10 cm (lower neutron flux), even at lower neutron fluence, implies that the compaction model may have some rate dependence that is not currently captured.

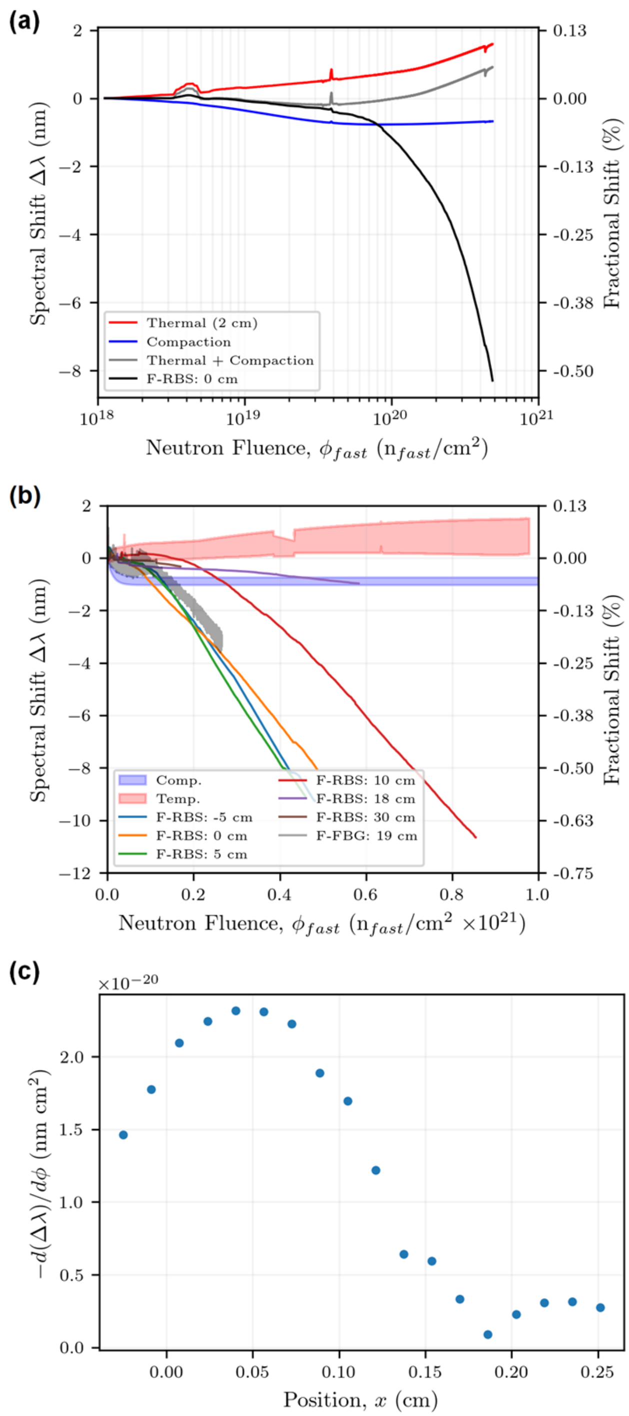

Fig. 4. (a) Measured spectral shift vs. fast neutron fluence (log scale) at 0 cm compared with expected shifts due to temperature and neutron-induced compaction effects. (b) Measured spectral shifts vs. fast neutron fluence (linear scale) at various positions compared with bounding values for spectral shifts caused by temperature changes and neutron-induced compaction. (c) Calculated spatial profile of $d(\Delta\lambda)/d\O$ obtained by fitting the spectral shift vs. neutron fluence data at high neutron fluence for each position along the F-RBS fiber.

4. Discussion

4.1 Signal transmission and backscatter amplitude

Increased backscatter amplitudes in the F-RBS fiber vs. the Ge-RBS fiber were expected based on previous findings [11], but the *enhanced* backscatter observed in the F-RBS fiber after reaching such a high neutron fluence was not expected. After ~2.3 days of effective full-power irradiation (~8×10^{19} n_{fast}/cm^2), contributions from Fresnel reflections would be negligible near the core midplane once the refractive index approached a uniform equilibrium value. At this point, the amplitude near the core midplane remained 1–2 dB higher than pre-irradiation values despite losses caused by upstream Fresnel reflections and any contributions from RIA. This result indicates that some other mechanism besides Fresnel reflections must be causing the increased amplitudes and that this mechanism dominates the effects of RIA. Backscatter amplitudes depend on the Rayleigh scattering coefficient α_R, which quantifies light scattering from random density fluctuations that are initially frozen during cooling following fiber drawing:

$$\alpha_R = \frac{8\pi^3}{3\lambda^4} n^8 p^2 k_B \beta T_f, \qquad (1)$$

where n, p, β, and T_F are the fiber's refractive index, photo-elastic coefficient, isothermal compressibility, and fictive temperature, respectively, and k_B is the Boltzmann constant.

Compaction-induced increases in refractive index as high as ~0.8% were previously reported [5]. With an 8^{th} power dependence on n, this increase in refractive index would increase the Rayleigh scattering coefficient by 6.6% (<0.3 dB), much less than the ~1.6 dB increase observed experimentally. The increases in backscattered amplitudes could also be explained by increases in T_F as local "thermal spikes" generated from neutron collision cascades are rapidly cooled from a higher temperature than the initial T_F that was established during fiber manufacturing [7]. For example, Leon et al. reported 12–20% increases in T_F following low neutron fluence (~10^{18} n/cm^2, no indication of neutron energy) irradiations of a-SiO_2 [26].

The combination of Fresnel reflections and enhanced RBS appears to explain most of the time and spatial dependences of the F-RBS amplitudes without considering the effects of RIA. Quantitative estimates of RIA were obtained by performing a linear fit of the amplitude vs. position data over select spatial positions along each fiber. The F-RBS data were fit from 0 to 20 cm, and the Ge-RBS data were fit from 35 to 45 cm. These positions were selected to avoid the effects of Fresnel reflections and end reflections (see Fig. 3). The RIA in F-RBS approached an equilibrium value of 2–4 dB/m, which is significantly less than previously reported values [12, 14] and is manageable for many sensor systems with a dynamic range of 20–40 dB and irradiated fiber lengths on the order of meters. By comparison, the Ge-RBS fiber suffered RIA >100 dB/m before the amplitudes reached the noise floor of the OBR system.

The F-FBG data show that gratings inscribed in the same fiber as F-RBS suffer significant reductions in amplitude (> 45 dB) that must be unrelated to RIA in the fiber itself due to the minimal RIA observed in the F-RBS fiber. The FBGs were inscribed using a femtosecond laser pulse to create a point-by-point modulation of the refractive index via a multiphoton absorption process to introduce defects in the glass network. Eventually, the atomic displacements generated from neutron-induced collision cascades dominate the defects that establish the local refractive index modulations within the FBG, thus effectively annihilating the grating. When the displacement damage dose approaches 1 dpa (~7×10^{20} n_{fast}/cm^2), all atoms that define the gratings statistically will have been displaced from their original atomic position. Fig. 2 shows that the F-

FBG amplitude approaches that of the F-RBS fiber (within 4 dB) after accumulating ~1.5×10^{20} n_{fast}/cm^2. The ~4 dB discrepancy is primarily caused by increased noise in the F-FBG fiber when the reactor is operating, as this discrepancy is much lower (<0.9 dB) post-irradiation. Therefore, the Type II FBGs tested herein provide no long-term benefit for OBR-based distributed fiber optic temperature sensing when compared with the F-RBS fiber.

4.2 Spectral shifts and implications on distributed temperature sensing

The large, unsaturated blue wavelength shifts that were observed in the pure silica core, F-doped silica cladding fibers are a concern for some sensing techniques, such as OBR, because these blue wavelengths shifts cause severe sensor drift. Blue wavelength shifts >10 nm (0.63%) correspond to a >1,000 °C decrease in temperature for a typical FBG temperature sensor with a sensitivity of 10 pm/°C near 1550 nm [27]. Uncertainties are not reported in Fig. 4 or the additional data in the Appendix, but the magnitude of the sensor drift is clearly a concern. It is difficult to quantify the uncertainties in the spectral shift data. Although uncertainty metrics have been proposed when performing cross-correlations of two spectral measurements [28], the adaptive reference techniques that were used here were only developed recently and methods for quantifying uncertainties using these approaches are still in development. The vendor of the OBR system tested herein quotes temperature uncertainties on the order of 0.1°C, which translates to a wavelength uncertainty of 1 pm. A previous study observed hysteresis in the range of 7 to 10°C (70 to 100 pm) after using adaptive reference techniques to recover spectral shifts during thermal testing to temperatures up to 1000°C [29]. This hysteresis may have resulted from error propagation using the adaptive reference techniques or from physical changes in the fiber itself. While there is no established approach to quantify uncertainties in the spectral shift data, the authors estimate the uncertainty to be on the order of tens of picometers.

The mechanism responsible for the unsaturated wavelength shifts is not currently known, but it is likely unrelated to radiation-induced compaction and changes in refractive index, as these parameters have been shown to reach an equilibrium in irradiated bulk materials [5]—some of which were irradiated to higher fast neutron fluences than the fibers tested in the present study [8]. Fig. 4(c) shows the spatial profile of the rate of change in spectral shift. These rates of change were determined from the slopes of the linear (high fluence) portions of the data in Fig. 4(b). The drift is most significant near 5 cm, which is closer to the maximum temperature location as opposed to the location with maximum neutron flux (approximately −5 cm). Therefore, the mechanism driving unsaturated blue wavelength shifts may have a strong temperature dependence. Additional information will be generated during post-irradiation examination of the fibers to better inform potential mechanistic explanations.

As mentioned previously, fused silica compaction has been shown to saturate at 2–3 vol% (0.67–1% linear compaction), which would cause a blue wavelength shift in the range of 10.3–15.5 nm after accumulating a fast neutron fluence >10^{20} n_{fast}/cm^2 [5-7]. However, the corresponding ~0.6–0.8% increase in refractive index partially offsets these blue wavelength shifts by including a positive (red) wavelength shift in the range of 9.3–12.4 nm. The net blue shifts predicted by the compaction model (see Fig. 4 and the detailed description in the Appendix) are <1 nm in magnitude. Indeed, previous works have measured blue wavelength shifts <1 nm following neutron irradiation to fast neutron fluences on the order of 10^{19} n/cm^2 [30]. Moreover, the compaction model generally agrees with the experimental data presented herein up to 10^{19} n/cm^2.

Although some gamma (or X-ray) irradiations and low neutron fluence (~10^{17} n/cm^2) irradiations have shown small (tens to hundreds of pm) red wavelength shifts [9], these tests did not subject the fibers to the significant displacement damage levels that are required to achieve saturation of the radiation-induced compaction. Zaghloul et al. observed unsaturated blue wavelength shifts in FBGs on the order of nanometers during neutron irradiation to fast neutron fluences on the order of 10^{20} n/cm^2 [16], which is consistent with the data obtained herein using fibers without FBGs that were tested to a higher neutron fluence. On the other hand, Fernandez et al. tested regenerated gratings (chemical composition gratings) written in a Ge/F-co-doped fiber to a fast neutron fluence of ~10^{19} n/cm^2 and observed a large red wavelength shift that reached saturation at ~14 nm [31].

The present results provide more fundamental data regarding spectral shifts in unaltered (no FBGs) fused silica fibers to help improve mechanistic understandings of radiation-induced compaction and its effect on sensor drift. The consistency between the results of Zaghloul et al. and the present study suggest that the regenerated FBGs tested by Fernandez et al. may have been affected by more complex chemical evolutions in the regenerated FBGs that would not be observed in Type II FBGs. In any case, it appears that higher neutron fluences on the order of 10^{20} n/cm^2 are required to observe the unsaturated drift phenomenon and the observed drift cannot be explained by radiation-induced changes in the fiber density and refractive index.

5. Summary and conclusions

This work used OBR to interrogate fiber optic sensors under extreme neutron irradiation to reveal several critical findings, which are summarized below. The results are encouraging for F-doped fiber optic signal transmission in extreme radiation environments but pose significant challenges to the use of OBR and other distributed sensing techniques given the large, unsaturated drift that was observed at high neutron fluence.

- Near-infrared (~1550 nm) RIA in Ge-doped fibers quickly becomes intolerable (>100 dB/m) at ~10^{19} n_{fast}/cm^2, whereas pure silica core, F-doped silica cladding fibers exhibit significantly lower RIA (2–4 dB/m) that approaches an equilibrium for fast neutron fluences up to ~10^{21} n_{fast}/cm^2.
- At high neutron fluence, the equilibrium RBS amplitude remains higher than pre-irradiation values, likely because of some combination of the compaction-induced increases in refractive index as well as increases in fictive temperature during rapid cooling from local “thermal spikes” generated during the displacement damage cascade.
- Type II FBGs inscribed in pure silica core, F-doped silica cladding fiber suffered >45 dB attenuation independent of RIA in the fiber once the defects that comprise the FBGs are annihilated by displacement damage. This shows that the Type II FBGs tested herein provide no long-term benefit for OBR-based distributed fiber optic temperature sensing in high-dose applications approaching 1 dpa.
- Reflected light signals from RBS and FBGs inscribed in pure silica core, F-doped silica cladding both indicate unsaturated blue wavelength shifts that cannot be explained by compaction effects or temporal temperature variations. Therefore, although the ability to transmit near-infrared light during extreme neutron fluence exposure is encouraging, the drift that would result from the unsaturated blue wavelength shifts is a major concern for some fiber optic–based sensors and may not be easily compensated for if the mechanism is unrelated to fused silica compaction.

6. Acknowledgements

This research was sponsored by the Nuclear Science User Facilities Program of the US Department of Energy (DOE), Office of Nuclear Energy. Data curation was supported by the Advanced Sensors and Instrumentation Program of the US DOE, Office of Nuclear Energy. Neutron irradiation in HFIR was made possible by the US DOE, Office of Science. Shay Chapel, Padhraic Mulligan, Kurt Smith, David Bryant, Bob Sitterson, Adam James, Maureen Searles, and Nora Dianne Ezell contributed to the design, analysis, assembly, and operation of the irradiation experiment.

7. References

[1] S. Girard, J. Kuhnhenn, A. Gusarov, B. Brichard, M.V. Uffelen, Y. Ouerdane, A. Boukenter, C. Marcandella, Radiation Effects on Silica-Based Optical Fibers: Recent Advances and Future Challenges, IEEE Trans. Nucl. Sci. 60(3) (2013) 2015–2036.

[2] D.L. Griscom, Optical Properties and Structure of Defects in Silica Glass, Journal of the Ceramic Society of Japan 99(1154) (1991) 923–942.

[3] L. Skuja, Optically active oxygen-deficiency-related centers in amorphous silicon dioxide, J. Non-Cryst. Solids 239(1) (1998) 16–48.

[4] L. Skuja, M. Hirano, H. Hosono, K. Kajihara, Defects in oxide glasses, physica status solidi (c) 2(1) (2005) 15–24.

[5] W. Primak, Fast-neutron-induced changes in quartz and vitreous silica, Physical Review 110(6) (1958) 1240.

[6] F. Piao, W.G. Oldham, E.E. Haller, The mechanism of radiation-induced compaction in vitreous silica, J. Non-Cryst. Solids 276(1-3) (2000) 61–71.

[7] W. Primak, Mechanism for the Radiation Compaction of Vitreous Silica, Journal of Applied Physics 43(6) (1972) 2745–2754.

[8] C.M. Petrie, A. Birri, T.E. Blue, High-dose temperature-dependent neutron irradiation effects on the optical transmission and dimensional stability of amorphous fused silica, J. Non-Cryst. Solids 525 (2019) 119668.

[9] A. Morana, E. Marin, L. Lablonde, T. Blanchet, T. Robin, G. Cheymol, G. Laffont, A. Boukenter, Y. Ouerdane, S. Girard, Radiation Effects on Fiber Bragg Gratings: Vulnerability and Hardening Studies, Sensors 22(21) (2022) 8175.

[10] F. Esposito, A. Srivastava, S. Campopiano, A. Iadicicco, Radiation Effects on Long Period Fiber Gratings: A Review, Sensors 20(9) (2020) 2729.

[11] E.J. Friebele, M.E. Gingerich, Radiation-induced optical absorption bands in low loss optical fiber waveguides, J. Non-Cryst. Solids 38-39 (1980) 245-250.

[12] T. Kakuta, T. Shikama, M. Narui, T. Sagawa, Behavior of optical fibers under heavy irradiation, Fusion Engineering and Design 41(1) (1998) 201–205.

[13] B. Brichard, A. Fernandez Fernandez, H. Ooms, F. Berghmans, M. Decréton, A. Tomashuk, S. Klyamkin, M. Zabezhailov, I. Nikolin, V. Bogatyrjov, E. Hodgson, T. Kakuta, T. Shikama, T. Nishitani, A. Costley, G. Vayakis, Radiation-hardening techniques of dedicated optical fibres used in plasma diagnostic systems in ITER, J. Nucl. Mater. 329-333 (2004) 1456-1460.

[14] G. Cheymol, H. Long, J.F. Villard, B. Brichard, High Level Gamma and Neutron Irradiation of Silica Optical Fibers in CEA OSIRIS Nuclear Reactor, IEEE Trans. Nucl. Sci. 55(4) (2008) 2252–2258.

[15] B. Brichard, P. Borgermans, A.F. Fernandez, K. Lammens, A. Decreton, Radiation effect in silica optical fiber exposed to intense mixed neutron-gamma radiation field, IEEE Trans. Nucl. Sci. 48(6) (2001) 2069–2073.

[16] M.A.S. Zaghloul, M. Wang, S. Huang, C. Hnatovsky, D. Grobnic, S. Mihailov, M.-J. Li, D. Carpenter, L.-W. Hu, J. Daw, G. Laffont, S. Nehr, K.P. Chen, Radiation resistant fiber Bragg grating in random air-line fibers for sensing applications in nuclear reactor cores, Opt. Express 26(9) (2018) 11775–11786.

[17] J. Wu, M. Wang, K. Zhao, S. Huang, M.A.S. Zaghloul, R. Cao, D. Carpenter, G. Zheng, S.D. Rountree, K.P. Chen, Distributed Fiber Sensors With High Spatial Resolution in Extreme Radiation Environments in Nuclear Reactor Cores, J. Lightw. Technol. 39(14) (2021) 4873-4883.

[18] D. Chandler, B.R. Betzler, E.E. Davidson, G. Ilas, Modeling and simulation of a High Flux Isotope Reactor representative core model for updated performance and safety basis assessments, Nucl. Eng. Des. 366 (2020) 110752.

[19] R.D. Cheverton, T.M. Sims, HFIR Core Nuclear Design, ORNL-4621, Oak Ridge National Laboratory, Oak Ridge, TN (1971).

[20] B.J. Soller, D.K. Gifford, M.S. Wolfe, M.E. Froggatt, High resolution optical frequency domain reflectometry for characterization of components and assemblies, Opt. Express 13(2) (2005) 666–674.

[21] M. Froggatt, J. Moore, High-spatial-resolution distributed strain measurement in optical fiber with Rayleigh scatter, Appl. Opt. 37(10) (1998) 1735–1740.

[22] D.C. Sweeney, A.M. Schrell, C.M. Petrie, An Adaptive Reference Scheme to Extend the Functional Range of Optical Backscatter Reflectometry in Extreme Environments, IEEE Sens. J. 21(1) (2020) 498–509.

[23] D.C. Sweeney, D.M. Sweeney, C.M. Petrie, Graphical Optimization of Spectral Shift Reconstructions for Optical Backscatter Reflectometry, Sensors 21(18) (2021) 6154.

[24] D.C. Sweeney, C.M. Petrie, Expanding the range of the resolvable strain from distributed fiber optic sensors using a local adaptive reference approach, Opt. Lett. 47(2) (2022) 269-272.

[25] M. Toulemonde, W.J. Weber, G. Li, V. Shutthanandan, P. Kluth, T. Yang, Y. Wang, Y. Zhang, Synergy of nuclear and electronic energy losses in ion-irradiation processes: The case of vitreous silicon dioxide, Physical Review B 83(5) (2011) 054106.

[26] M. León, L. Giacomazzi, S. Girard, N. Richard, P. Martín, L. Martín-Samos, A. Ibarra, A. Boukenter, Y. Ouerdane, Neutron Irradiation Effects on the Structural Properties of KU1, KS-4V and I301 Silica Glasses, IEEE Trans. Nucl. Sci. 61(4) (2014) 1522-1530.

[27] K.O. Hill, G. Meltz, Fiber Bragg grating technology fundamentals and overview, J. Lightw. Technol. 15(8) (1997) 1263–1276.

[28] R. Misra, A. Bora, G. Dewangan, Estimation of error on the cross-correlation, phase and time lag between evenly sampled light curves, Astronomy and Computing 23 (2018) 83-91.

[29] J.T. Jones, D.C. Sweeney, A. Birri, C.M. Petrie, T.E. Blue, Calibration of distributed temperature sensors using commercially available SMF-28 optical fiber from 22°C to 1000°C, IEEE Sens. J. 22(5) (2022) 4144-4151.

[30] G. Cheymol, L. Remy, A. Gusarov, D. Kinet, P. Mégret, G. Laffont, T. Blanchet, A. Morana, E. Marin, S. Girard, Study of Fiber Bragg Grating Samples Exposed to High Fast Neutron Fluences, IEEE Trans. Nucl. Sci. 65(9) (2018) 2494–2501.

[31] A.F. Fernandez, B. Brichard, F. Berghmans, H.E. Rabii, M. Fokine, M. Popov, Chemical composition fiber gratings in a high mixed gamma neutron radiation field, IEEE Trans. Nucl. Sci. 53(3) (2006) 1607-1613.

Appendix

Methods. Fig. A1 shows the spatial variations in fast neutron fluence and dose at the end of the experiment, for positions along each fiber > −10 cm. Fig. A2 shows the time evolution of the reactor power, with initial low-power operations at ~10 MW followed by continuous operation at 85 MW for approximately 25 total days. After ~10 days of full-power operation, the reactor was shut down for several days before returning to full power. Fig. A3 shows temporal and spatial variations in temperature, as measured by the thermocouples, throughout the duration of the irradiation experiment.

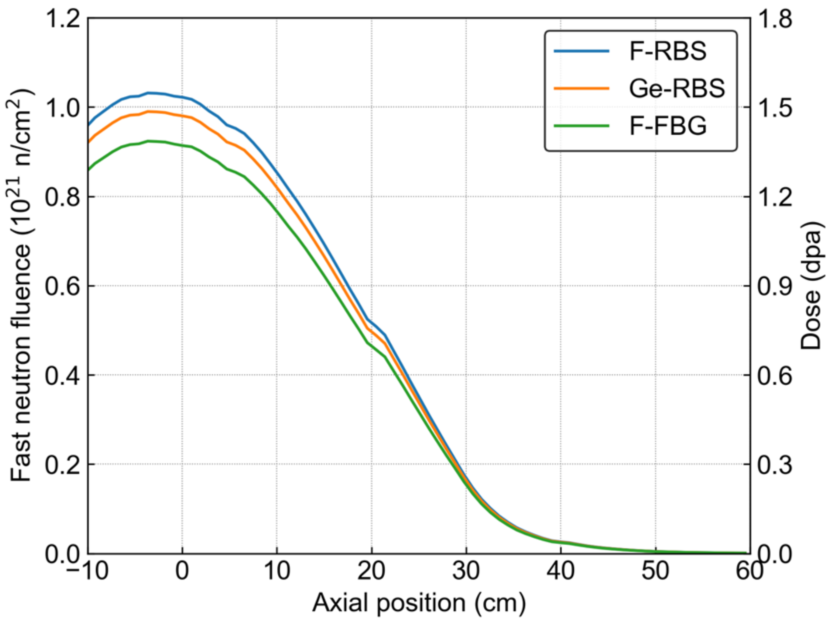

Fig. A1. Axial fast neutron fluence profiles for each fiber at the end of the irradiation testing. The positions shown are relative to the midplane of the reactor core. The peak neutron fluence occurs below the reactor midplane due to shifts in neutron flux that occur over the duration of the reactor cycle as the control plates are withdrawn.

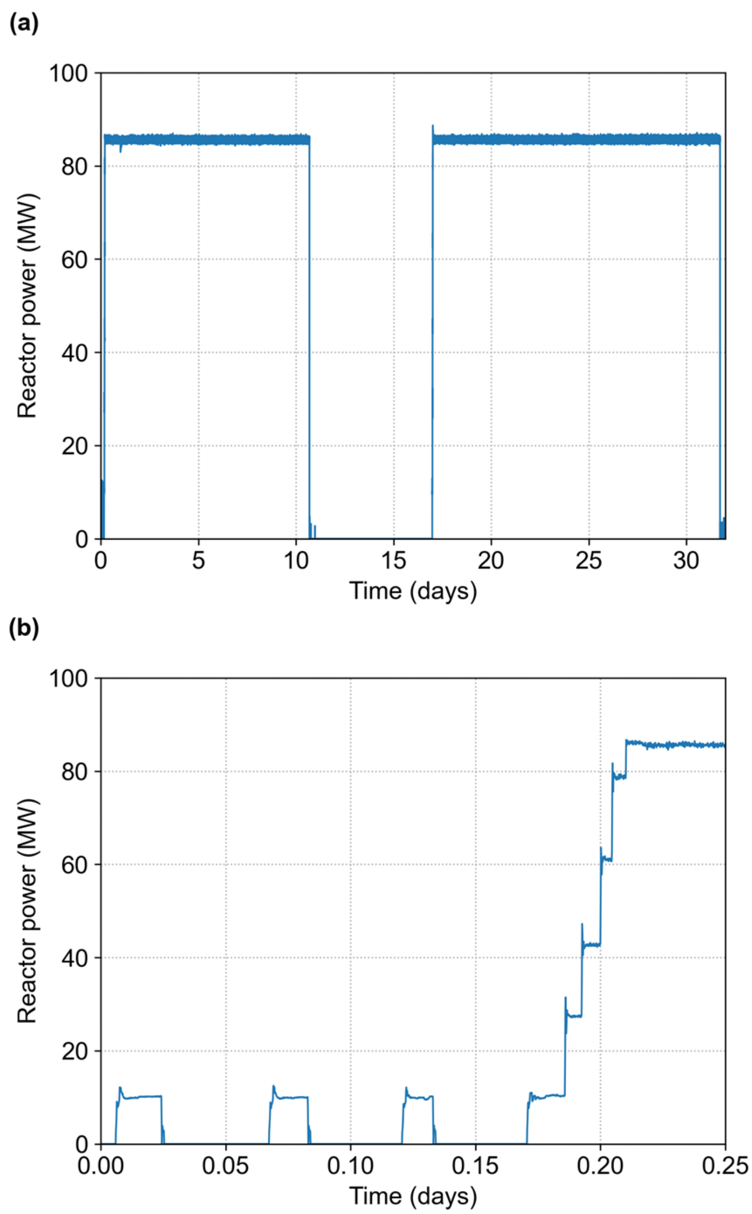

Fig. A2. Time evolution of the reactor power showing (a) the entire operating history and (b) the initial startup operations.

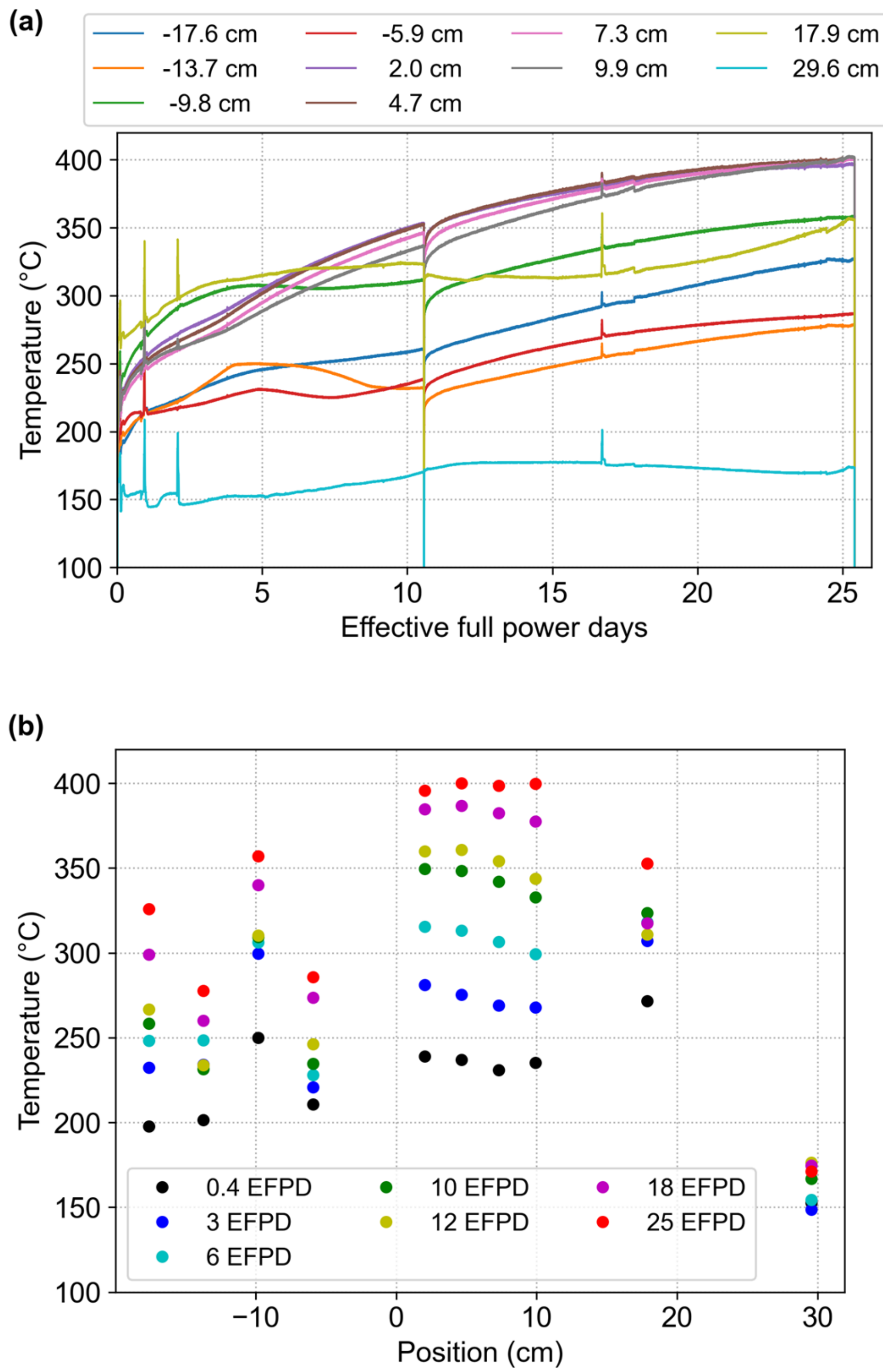

Fig. A3. (a) Time evolution of the experiment temperatures measured by thermocouples at various locations relative to the core midplane and (b) the spatial temperature profiles after various effective full-power days (EFPDs) of irradiation.

Analysis. The wavelength shifts that would be expected due to the effects of compaction were determined using a previously established model that determines the volumetric compaction (C) in a-SiO_2 as a function of temperature (T, in Kelvin) and fast neutron fluence (Φ in n_{fast}/cm^2) [1]:

$$C(\Phi,T) = C_\infty(T)\left(1 - e^{-\frac{\Phi}{\Phi_S(T)}}\right), \qquad \text{(A1)}$$

$$C_\infty(T) = 0.023 + 6.30 \times 10^{-6}T - 2.60 \times 10^{-8}T^2, \qquad \text{(A2)}$$

$$\Phi_S(T) = 3.42 \times 10^{19}\frac{n}{cm^2}exp(-\frac{0.036\ eV}{kT}), \qquad \text{(A3)}$$

where $k = 8.617 \times 10^{-5}$ eV/K is the Boltzmann constant.

The wavelength shift ($\Delta\lambda$) caused by compaction is calculated as

$$\Delta\lambda(\Phi,T) = \lambda\left[-\left(\frac{C(\Phi,T)}{3}\right) + \left(\frac{\Delta n}{n}\right)\right], \qquad \text{(A4)}$$

where λ is the initial wavelength (1550 nm) and Δn is the change in the refractive index caused by radiation-induced compaction effects.

The $\frac{\Delta n}{n} = \frac{n(\Phi,T) - n(0,20°C)}{n(0,20°C)}$ term was calculated from correlations between the refractive index and density ($\rho(\Phi,T) = 2.20[1 - C(\Phi,T)]$ g/cm^3) developed by Kitamura et al. for evaluating densified silica glass based on extended point dipole theory [2]:

$$n(\Phi,T) = \sqrt{1 + \frac{4\pi\rho(\Phi,T)}{M}\sum_i \frac{A_i B_i(\Phi,T)\lambda^2}{\lambda^2 - B_i(\Phi,T)\lambda_i^2}}, \qquad \text{(A5)}$$

$$B_i(\Phi,T) = \frac{1}{1 - \frac{b_i A_i \rho(\Phi,T)}{M}}, \qquad \text{(A6)}$$

where $M = 60.084$ g/mol is the molecular weight of SiO_2. The constants B_i depend on Φ and T because of the dependence on $\rho(\Phi,T)$ in Equation (A6). The constants A_i, b_i, and λ_i are summarized in Table A1 (taken from Kitamura et al. [2]).

Table A1. Previously determined parameters [2] used for determining radiation-induced changes in refractive index and their effect on local wavelength shifts.

Parameter	$i = 1$	$i = 2$	$i = 3$
A_i (cm^3/mol)	1.483564	0.583781	6.067029
b_i	3.084249	2.684692	-15.582117
λ_i (μm)	0.068149	0.118332	17.624056

Fig. A4 and Fig. A5 provide more detail regarding the measured local shifts in the reflected wavelength from the F-RBS fiber vs. fast neutron fluence at multiple locations relative to the reactor core midplane. Both figures show the same data, but the fast neutron fluence data are shown on different scales (linear vs. log scale) to provide more detail at both low and high neutron fluence. Wavelength shifts are relative to the times when the reactor reached full power and do not account for shifts during reactor startup or shutdown. The estimated wavelength shifts caused by changes in temperature and radiation-induced compaction are also shown. The wavelength shifts that would be expected due to temperature changes were estimated by determining the change in temperature measured by the closest thermocouple and multiplying by a temperature coefficient of 10 pm/°C [3]. The disagreement between the measured vs. estimated wavelength shifts at 18 and 30 cm could be related to the larger spatial temperature variations in these positions and the fact that the fiber optic sensors and thermocouples may have been exposed to different temperatures.

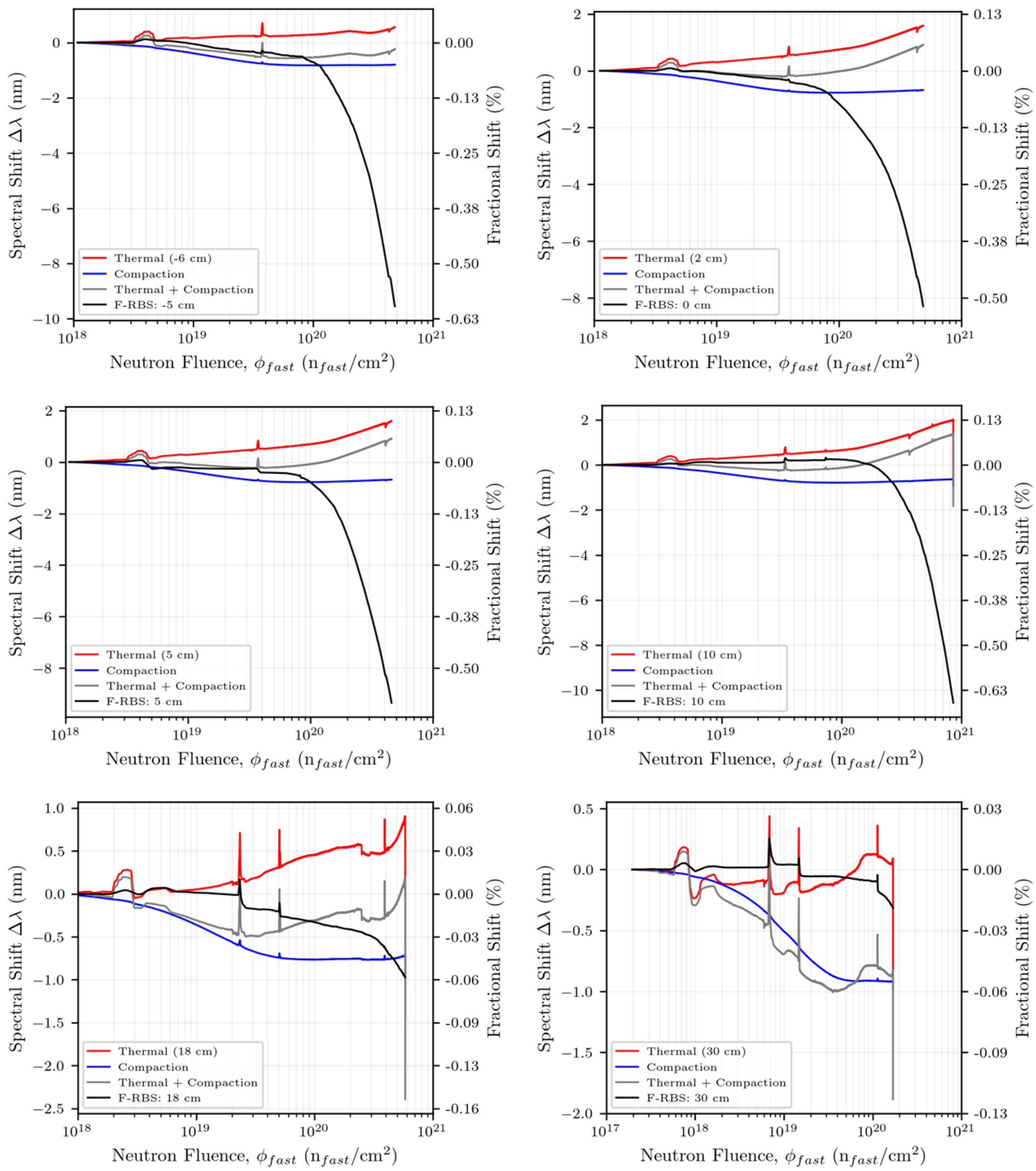

Fig. A4. Measured spectral shift vs. fast neutron fluence (log scale) for various positions from the F-RBS fiber. Data are compared with expected shifts due to temperature and neutron-induced compaction effects.

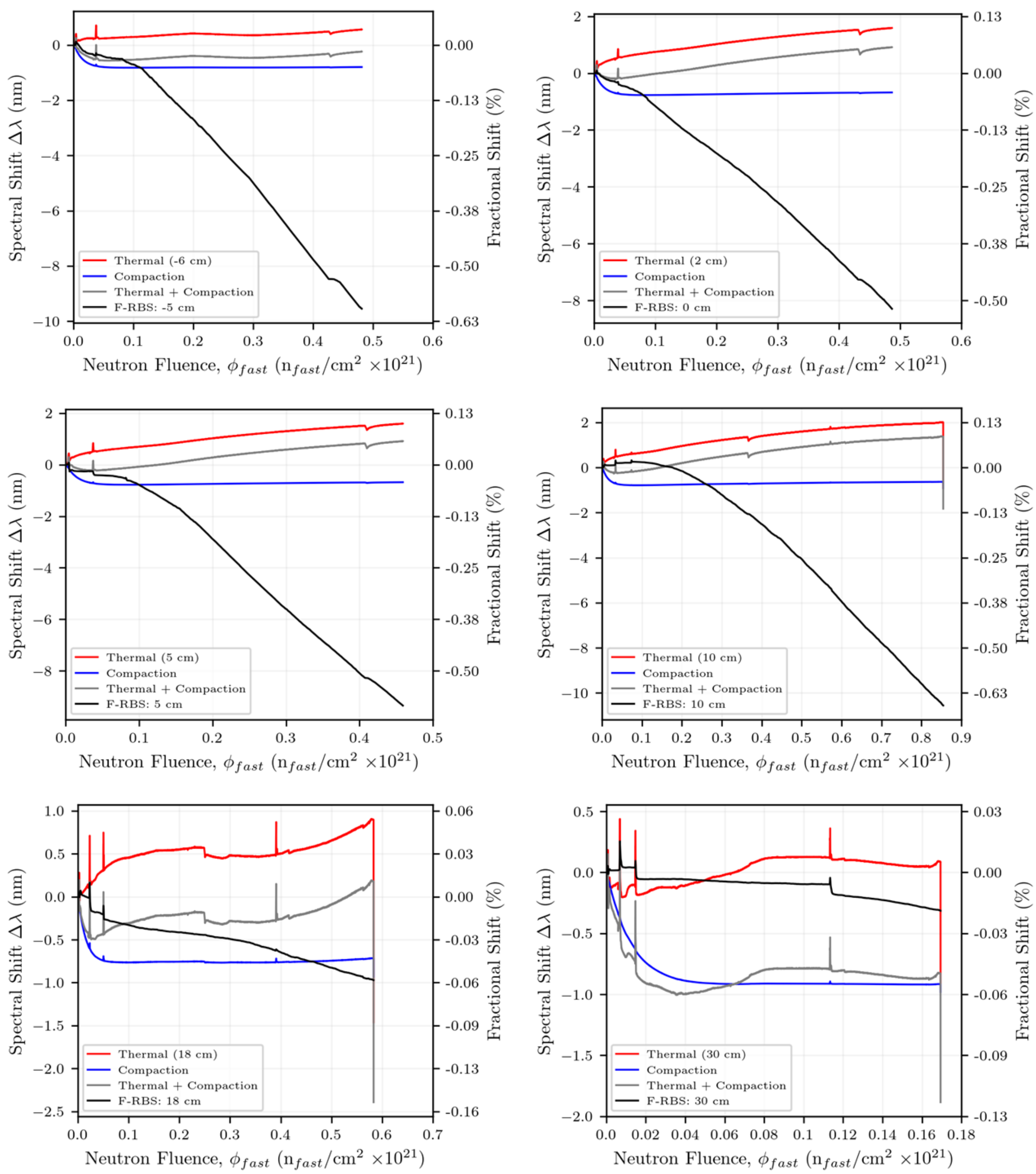

Fig. A5. Measured spectral shift vs. fast neutron fluence (linear scale) for various positions from the F-RBS fiber. Data are compared with expected shifts due to temperature and neutron-induced compaction effects.

References

[1] C.M. Petrie, A. Birri, T.E. Blue, High-dose temperature-dependent neutron irradiation effects on the optical transmission and dimensional stability of amorphous fused silica, J. Non-Cryst. Solids 525 (2019) 119668.
[2] N. Kitamura, Y. Toguchi, S. Funo, H. Yamashita, M. Kinoshita, Refractive index of densified silica glass, J. Non-Cryst. Solids 159(3) (1993) 241–245.

[3] K.O. Hill, G. Meltz, Fiber Bragg grating technology fundamentals and overview, J. Lightw. Technol. 15(8) (1997) 1263–1276.